A Reconfigurable Two-stage 11kW DC-DC Resonant Converter for EV Charging with a 150-1000V Output Voltage Range

Bram Oude Aarninkhof, Dingsihao Lyu, *Member, IEEE*, Thiago Batista Soeiro, *Senior Member, IEEE*, Pavol Bauer, *Senior Member, IEEE*

Abstract—In this paper, a reconfigurable two-stage DC/DC resonant topology with a wide output voltage range of 150-1000 V is proposed for Electric Vehicle (EV) charging with high efficiency over the entire load range. The proposed topology consists of an LLC resonant converter with dual secondary sides; two interleaved triangular current mode buck converters, and three additional auxiliary switches for reconfiguration. Two possible arrangements of the proposed topology are considered and compared. The analytical model of the topology is developed, which is used for the efficiency estimation of different configurations and the design of the prototype converter. An 11 kW hardware demonstrator is built and tested. The maximum measured efficiency of the converter is **97.66%**, with a **>95% efficiency** over the complete 150-1000 V range at full power. The proposed two-stage converter achieves the widest output voltage range reported in literature for resonant power converters, thereby capable of charging existing and future EVs very efficiently over any charging cycle.

Index Terms—DC-DC converters, resonant converter, wide output voltage range, EV, LLC, EV charger, TCM buck

I. INTRODUCTION

THE electrification of the world's transportation fleet has gained momentum in recent years. For example the widespread use of Electric Vehicles (EVs) today. This shift to EVs is all in light of a global effort to reduce Global Greenhouse Gas (GHG) emissions [1]. Consequently, the demand for public EV chargers to accommodate all these vehicles will increase correspondingly. According to the Sustainable Development Scenario (SDS) [2], 6% of the electricity consumption in the European Union in 2030 will come from EV charging, compared to 0.2% in 2019.

Most EVs currently produced use a battery pack with a nominal voltage of 400 V. However, in recent years, some models have been announced that use a higher voltage battery architecture [3]. This higher battery voltage which is typically close to 800 V can be one of the solutions enabling a faster charging time of EVs [25].

The introduction of these higher voltage battery architectures imposes a challenge on the EV chargers: the (common) 400 V battery architecture as well as the new high voltage battery architectures need to be accommodated. As a result, the typical DC/DC converters used in the EV chargers must operate in an extremely wide output voltage range.

However, few studies in literature have provided experimentally verified isolated DC/DC converter designs that are able to charge both the 400V and 800V EVs, though Lyu

et al. (2022) proposed a reconfigurable Phase Shifted Full Bridge (PSFB) to achieve this wide output voltage range [15]. For Resonant Power Converters (RPC), no such large output voltage range has been achieved [6]–[11], [13], [14], [27]–[64]. Based on the studies about the resonant converters in the EV charging application in the past decade (2010-2021), Figure 2 shows the reported output voltage ranges of the RPCs. Most of the studies report an output voltage range between 250-450 V, corresponding with the typical battery voltage of a 400 V battery architecture. Seven studies reported an output voltage range of ΔV_o >320 V [5]–[11].

The challenge lies in the poor efficiency performance when these converters are made to operate in such a wide voltage range. The RPC is typically controlled by frequency modulation, and it is well-known for its high-efficiency performance when it is operated at the resonant frequency point. However, operating the RPCs with frequency modulation in a wide output voltage range will result in a wide switching frequency range, which brings the issues of more complicated magnetic component design, a decrease in efficiency and reduced EMI performance [12]. As a result, the conventional RPC, such as an LLC converter, is not able to provide high efficiency in a wide voltage range application.

To extend the output voltage conversion range of the RPCs without compromising the system efficiency performance in the whole operational range, mainly five methods can be found in the literature. The first method uses a variable input DC link voltage while operating the RPC in the resonant frequency point [5], [6]. The output voltage regulation of the RPC using this method is entirely performed by the variable input voltage. The direct benefit of this method is that the RPC is operated at the maximum efficiency point with simple fixed frequency modulation. However, this method requires a controlled front-end converter which provides the adjustable input DC link voltage for the RPC. As a result, the design and implementation complexity shift from the RPC converter to the front-end converter.

The second method is based on having two RPC converters operating in an interleaving way. Both switch at the resonant switching frequency, and they are phase-shifted to control the output voltage [9]. This method operates the RPCs with constant switching frequency, which is easy to implement and provides ZVS and high efficiency for the individual RPCs. However, due to the increase of circulating current-induced conduction loss, the interleaved RPC has a significant

(a) Configuration I: S_{aux} after the interleaved BUCK stage (selected)

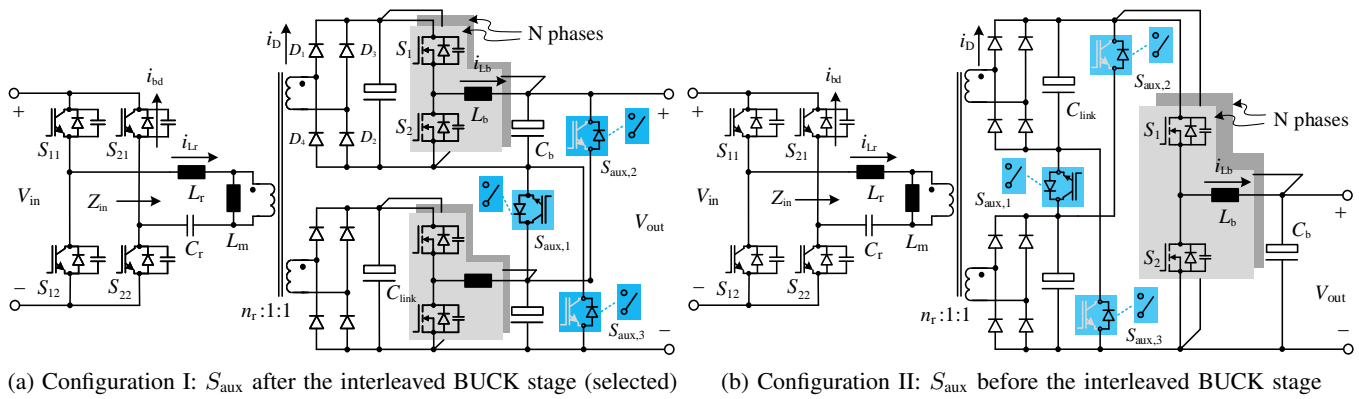(b) Configuration II: S_{aux} before the interleaved BUCK stage

Fig. 1: The schematics of the proposed reconfigurable two-stage Resonant Power Converter (RPC) in two different arrangements. Note that $S_{aux,1/2/3}$ can be either mechanical switches or semiconductor transistors.
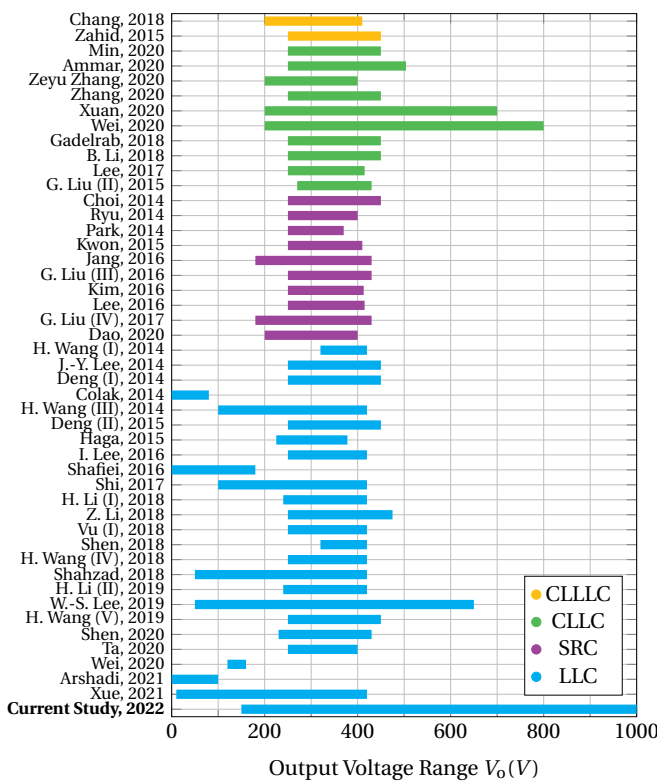

Fig. 2: Overview of the output voltage range of all studies found regarding Resonant Power Converters and EV charging from 2014-2022 [6]–[11], [13], [14], [27]–[64].

efficiency drop when the output voltage is low.

The third method uses a three-level bidirectional RPC together with Pulse Frequency Modulation (PFM), often abbreviated as; frequency modulation [8]. This RPC features two pairs of three-level full bridges, a resonant inductor and a capacitor. By combining the four operational modes of each of the three-level full bridges, this three-level bidirectional RPC adapts to a wide output voltage range with a small range of switching frequency change. However, the trade-off is the cost of the converter and control complexity, as it requires a total of 16 transistors.

The fourth method is to use a flexible voltage gain control scheme for the full-bridge resonant converter, for example, proposed by Wei et al. (2020) [7]. A flexible voltage gain control could be a combination of reconfiguration between full-bridge and half-bridge of the switching bridge [66], a variable DC-link voltage provided by the grid-connected circuit and/or series compensation capacitance [67], Phase Shift Modulation (PSM) which results in a controllable duty cycle of the H-bridge inverter, and dual control where both frequency modulation and PSM are implemented together [26]. These approaches extend the voltage range by the increased control complexity without modification on the converter topology.

The fifth method uses a two-stage structure, where the RPC is the first stage, followed by a buck converter as the second stage [11]. This two-stage solution allowed for a decoupling of the functions of the proposed converter: the resonant stage provides galvanic isolation and a constant voltage step-up through the turns ratio of the transformer. Only the buck converter controls the output voltage since the LLC is operated only at the resonant frequency. Consequently, this approach achieves a wide voltage regulation range with a simple control scheme due to the control decoupling of the two stages. However, the drawback is higher cost, and the efficiency performance depends on this additional stage.

A comparison of all studies regarding wide output voltage range RPCs is given in Table I. It can be seen that, in the case of designing an RPC for wide voltage regulation when bidirectional operation is not a necessity, the two-stage approach is the conventional way to be implemented. The RPC stage can operate at a constant frequency near the series resonant frequency, allowing for optimal design of the magnetic components and minimal losses. Besides this, ZVS of the primary switches is guaranteed for the entire operating range. However, the efficiency performance of the two-stage solution still has room for improvement. When a simple continuous conduction mode (CCM) buck converter is used for the voltage regulation stage, the efficiency is limited by mainly two factors, namely the turn-on switching loss and the low duty cycle when the output voltage is low. As a result, the two-stage RPC converter will suffer from a considerable efficiency drop during; moments of heavy load where the

TABLE I: Comparison of all wide output voltage range solutions involving an RPC.

	Variable input voltage SEPIC PFC + LLC [5]	Variable input voltage SEPIC PFC + LLC [6]	Two interleaved LLC converters [9]	Three level CLLC Converter [8]	Combination of Control Strategies CLLC converter [7]	Two-Stage: LLC + buck converter [11]
Modulation	Constant f_{sw}, Variable V_{in}	Constant f_{sw}, Variable V_{in}	PSM	PFM + Variable operational modes	PFM + Variable V_{in} + reconfig. HB or FB	LLC: Constant f_{sw} buck: Duty cycle
Output Voltage range	100-420 V	100-420 V	10-420 V	200-700 V	200-800 V	50-650 V
Switching frequency range	-	200 kHz	100 kHz	31-70 kHz	140-250 kHz	120 kHz & 50 kHz
Number of switches	5	5	4	16	8	5
Number of Diodes	9*	9*	4	4	0	9
Number of Transformers	1	1	2	1	1	2
Peak efficiency	97.4%	88.4%	98.10%	96.8%	98.5%	97.32%
Maximum Power	3.3 kW	3.3 kW	1 kW	3.5 kW	22 kW	20 kW
Control Complexity	Moderate	Moderate	Moderate	Complex	Complex	Simple
Power Density	-	-	-	-	8 kW/L	-

turn-on switching loss is high, and moments when the output voltage, and thus the equivalent duty cycle, is low.

Commercial solutions for wide output voltage EV charging are available, such as the ABB Terra 53/54 50kW, ENERCON E-charger 600 [69], ABB Terra 184 CC HVC and Porsche Charge Box [70]. The proposed topology has not been used in the commercially available EV chargers of which the topology is known [69] [70]. On top of that, none of these EV chargers use an isolated topology which would be likely to achieve high efficiencies over the entire output voltage and power range, which makes the proposed two-stage converter unique.

This paper proposes a new two-stage reconfigurable LLC resonant converter cascaded with interleaved Triangular Current Mode (TCM) buck converter to address the shortcomings. Figure 1 shows the two possible configurations of the proposed converter. This converter is capable of a wide output voltage range operation (150-1000 V) that enables the charging of both the 400V and 800V EVs. The LLC full-bridge converter stage is operated at the resonant frequency to benefit from the high efficiency and easy design. By having the interleaved TCM buck converter for the second stage, the turn-on switching loss can be eliminated and the efficiency can be improved due to ZVS [18]. The interleaving also reduces the current stresses (and thereby conduction losses) for the individual TCM buck converter [19], and it allows the large output current ripple of a single TCM buck converter to be partially attenuated, reducing the required DC-link output capacitance. Moreover, the reconfigurable structure allows the secondary sides to be connected in parallel or in series, depending on the output voltage conditions [15]. With this structure, the interleaved buck converter can be operated with a high duty cycle even when the output voltage is low, which results in higher efficiency performance.

The contribution of this paper is as follows:

1) A two-stage LLC converter cascaded with interleaved TCM buck converter with a reconfigurable structure is proposed in this paper, allowing for a wide output voltage range while maintaining high efficiency over the entire load range.

2) The complete design guidelines including the steady-stage analytical model of the converter are presented. The two possible arrangements and the choice of transistor technologies for the proposed converter are comprehensively evaluated.

3) The proposed converter is experimentally verified, and the performance benchmark of the proposed converter and the conventional frequency modulated LLC converter for the wide output voltage range (150-1000V) EV charging application is presented. This design benchmark is particularly important because it identifies the proposed converter as an outstanding solution for the future EV market without compromising efficiency.

The structure of the rest of the paper is as follows. Section II Section II discusses the operating principle of the proposed two-stage converter. Furthermore, in Sections III and IV, the steady-state analytical models of both the LLC converter and the Interleaved TCM buck converter are presented, respectively. The details regarding the design of both converters are presented in Section V. The results of the analytical comparison of the two possible configurations of the two-stage converter based on the analytical models are presented in Section VI. In Section VII a comparison is made between the proposed converter and the conventional LLC operating using PFM, which is called rLLC PFM in this paper. And finally, the results of the experimental verification of the selected configuration are presented in Section VIII.

II. OPERATING PRINCIPLE OF THE TWO-STAGE CONVERTER

One of the enablers of the wide output voltage range two-stage converter proposed in this study is the Voltage-Doubler/Current-Doubler (VD/CD) reconfigurable structure. This structure allows to either connect the two TCM buck outputs in series (to achieve between 500-1000 V) to charge the 600 V or 800 V batteries, or in parallel (to achieve 150-500 V) to charge the 400 V or lower voltage batteries. And this

flexibility in connection is beneficial because the efficiency of the buck converter decreases with decreasing duty cycle D, and the range of the duty cycle during the charging process can be reduced by half by using the VD/CD reconfigurable structure. Consequently, this structure allows the maximum efficiency to be achieved twice in the whole output voltage range. This is especially advantageous since both the $400\,\text{V}$ as well as the $800\,\text{V}$ battery architectures can be charged with similarly high efficiency.

The operating principle of the reconfigurable structure is as follows: during the communication period in an EV charging session, the EV will inform the charger about the required charging voltage and current value [65]. By comparing the voltage value to a preset boundary voltage value V_{re}, the proposed two-stage LLC converter can be configured into a parallel connection configuration if the required charging voltage value is lower than $500\,\text{V}$ or as a series connection if the value is higher than $500\,\text{V}$, by setting the states of the auxiliary switches $S_{\text{aux,1,2,3}}$. This connection configuration is done before the start of the charging session, and thus the commutation occurs at zero current.

If there are EVs with a voltage range across 500V, the sudden change of capacitor voltage due to the dynamic reconfiguration can be avoided by implementing a simple shutdown–reconfiguration-restart mechanism in the controller of the charger. During the energy transferring process, the communication between the vehicle and the charger is still on, and the vehicle continues to send a setting value of charging current or voltage to the DC EV charging station throughout the charging process [65]. Once the charging voltage reaches 500V, which is the reconfiguration value of the converter, the charger executes a shutdown process. Once the shutdown process is finished, the charging current is zero, and the contactors of the DC power lines are open, the converter can be configured from the parallel connection into the series connection. Then the energy transferring process is resumed. Another approach is that the conventional frequency modulation can be implemented in the LLC converter stage. By adjusting the switching frequency the converter can cover the exceeding battery voltage range.

The two settings of the auxiliary switches are described below:

Series connection: When $S_{\text{aux,1}}$ is kept on while $S_{\text{aux,2,3}}$ are maintained off, the negative rail of the upper converter transformer's secondary-side rectifier is connected with the positive rail of the lower side converter rectifier, making the two secondary side circuits connected in series. This configuration enables the converter to supply high output voltage with the utilization of diodes and capacitors with halved voltage rating compared to those of the conventional approach.

Parallel connection: When $S_{\text{aux,1}}$ is kept off while $S_{\text{aux,2,3}}$ are maintained on, both the transformer's secondary side rectifiers of the converters are connected in parallel. This configuration enables the converter to operate in the low output voltage range $<500\,\text{V}$.

Two locations exist where the VD/CD structure can be implemented: After the Interleaved TCM buck converter (Configuration I), or after the LLC converter (Configuration II).
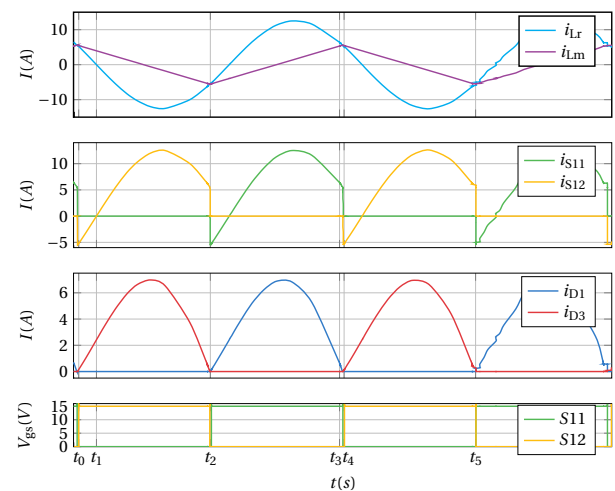

Fig. 3: Operational waveforms of the LLC converter, which is the first stage in the proposed two-stage converter. The series resonant current i_{Lr} and magnetizing current i_{Lm} are given in the top graph, i_{S1} and i_{S2} are the drain-to-source currents of S11 and S12, respectively, and currents through diode D1 and D3 are given in the third graph. The final graph shows the gate-to-source voltage V_{gs} of S11 and S12. See Figures 1a and 1b for reference.

See Figures 1a and 1b, respectively, for a schematic of both Configurations.

The VD/CD structure can be either implemented with solid-state switches or mechanical relays. A benchmarking between both circuits shown in Figures 1a and 1b will be presented in Section VI. First, the analytical models of the LLC converter and TCM buck converter are presented in Section III and Section IV, respectively.

III. STEADY STATE ANALYTICAL MODELLING OF THE LLC CONVERTER

The LLC converter operates at a fixed switching frequency slightly above the series resonant frequency $f_{\text{sr}} = 1/\sqrt{(L_{\text{r}}C_{\text{r}})}$. A simplified analysis technique to represent the LLC converter operating close to f_{sr} is the Fundamental Harmonic Approximation (FHA) [20]. This approximation enables classic AC analysis to be used by reducing the entire secondary side of the LLC converter to an equivalent AC resistance R_{AC}.

All equations regarding the LLC converter are listed in Table II. R_{L} is the load resistance after the rectifier, which is given by (2) for this two-stage converter. The input impedance Z_{in} can be seen as the impedance seen from the primary side full bridge towards the secondary side. For an explanation of M_{v}, Z_{o} and Q_{L} the reader is referred to [20]. The rest of the parameters given in Table II can be found in Figure 1.

Figure 3 shows the typical operational waveforms of the LLC converter in resonant frequency.

A. Soft Switching

The LLC converter can achieve ZVS turn-on of the primary side switches. Due to the operation of the converter just

TABLE II: All equations on which the analytical model of the LLC converter is based.

Description	Parameter	Equation	
Equivalent AC Resistance	R_{AC}	$\frac{8n^2 R_L}{\pi^2}$	(1)
Equivalent load resistance	R_{L}	$\frac{(2 \cdot V_{\mathrm{link}})^2}{P_o}$	(2)
Voltage gain	M_{v}	$\frac{1}{\sqrt{\left(1+l-l\cdot\left(\frac{\omega_0}{\omega}\right)^2\right)^2 + Q_L^2 \cdot \left(\frac{\omega}{\omega_0} - \frac{\omega_0}{\omega}\right)^2}}$	(3)
Inductance Ratio	l	$\frac{L_{\mathrm{r}}}{L_{\mathrm{m}}}$	(4)
Characteristic Impedance	Z_{o}	$\sqrt{\frac{L_r}{C_r}}$	(5)
Quality Factor	Q_{L}	$\frac{Z_0}{R_{\mathrm{AC}}}$	(6)
Amplitude of Input Impedance	$|Z_{\mathrm{in}}|$	$\sqrt{\frac{64 L_m^2 R_L^2 n^4}{64 R_L^2 n^4 L_r C_r + L_m \pi^2}}$	(7)
Angle of Input Impedance	$\angle Z_{\mathrm{in}}$	$\arctan\left(\frac{8\sqrt{L_r C_r}n^2}{L_m \pi^2}\frac{V_o^2}{P_o}\right)$	(8)
Series Inductor RMS current	$I_{\mathrm{Lr,RMS}}$	$\frac{4}{\pi}\frac{1}{\sqrt{2}}\frac{V_{\mathrm{in}}}{|Z_{\mathrm{in}}|}$	(9)
Magnetizing RMS current	$I_{\mathrm{Lm,RMS}}$	$\frac{4V_{\mathrm{in}}}{\pi\sqrt{2}}\frac{M_{\mathrm{v}}}{\omega L_m}$	(10)
Maximum resonant Capacitor voltage	$V_{\mathrm{Cr,max}}$	$\frac{1}{\omega C_r}\sqrt{2}I_{\mathrm{Lr,RMS}}$	(11)
Switch turn-on current	$I_{\mathrm{Sx,on}}$	$-\sqrt{2}I_{\mathrm{Lr,RMS}}\sin(\angle Z_{\mathrm{in}})$	(12)
Switch turn-off current	$I_{\mathrm{Sx,off}}$	$\sqrt{2}I_{\mathrm{Lr,RMS}}\sin(\angle Z_{\mathrm{in}})$	(13)
RMS switch current	$I_{\mathrm{Sx,RMS}}$	$\frac{\sqrt{2}I_{\mathrm{Lr,RMS}}}{2\sqrt{\pi}}\sqrt{\cos(\angle Z_{\mathrm{in}})\sin(\angle Z_{\mathrm{in}})+(\pi-\angle Z_{\mathrm{in}})}$	(14)
Average switch current	$I_{\mathrm{Sx,avg}}$	$\sqrt{2}I_{\mathrm{Lr,RMS}}\frac{\cos(\angle Z_{\mathrm{in}})+1}{2\pi}$	(15)
RMS switch bodydiode current	$I_{\mathrm{bd,RMS}}$	$\frac{\sqrt{2}I_{\mathrm{Lr,RMS}}}{2\sqrt{\pi}}\sqrt{-\cos(\angle Z_{\mathrm{in}})\sin(\angle Z_{\mathrm{in}})+\angle Z_{\mathrm{in}}}$	(16)
Average switch bodydiode current	$I_{\mathrm{bd,avg}}$	$\sqrt{2}I_{\mathrm{Lr,RMS}}\frac{\cos(\angle Z_{\mathrm{in}})-1}{2\pi}$	(17)
Average 'rectifier Diode' current	$I_{\mathrm{D,avg}}$	$\frac{1}{2}\frac{P_o}{V_{\mathrm{link}}}$	(18)
RMS 'rectifier Diode' current	$I_{\mathrm{D,RMS}}$	$\frac{\pi}{2}I_{\mathrm{D,avg}}$	(19)
RMS DC-link capacitor current	$I_{\mathrm{Clink,RMS}}$	$\frac{1}{2}\frac{P_o}{V_o}\sqrt{\frac{\pi^2}{8}-1}$	(20)

above f_{sr}, where the input impedance of the Resonant Tank Network (RTN) is inductive, ZVS is achieved in all primary side switches for the entire load range of the LLC converter.

The maximum magnetizing inductance L_{m} that allows the output capacitances to be completely charged/discharged within a given deadtime is given by (21) [21].

$$L_{\mathrm{m,max}} = \frac{t_{\mathrm{dead}}}{16 \cdot C_{\mathrm{equi}} f_{\mathrm{sw}}} \tag{21}$$

Where C_{equi} is the equivalent representation of all output capacitances C_{oss}. Which is calculated based on the method proposed by Kasper et al. (2016) [22].

$$C_{\mathrm{equi}} = 4 \cdot C_{\mathrm{oss}} \tag{22}$$

IV. Steady State Analytical Modelling of the Interleaved TCM buck converter

The TCM buck is a synchronous buck converter, as shown in Figure 5. All equations of the analytical model of the TCM buck converter used in this paper are given in Table III.

Figure 4 shows the typical operational waveforms of a TCM buck converter. In the top graph of Figure 4 it can be observed that the current through the inductor I_{Lb} can reverse its direction (become negative). The current continues to turn negative until $I_{\mathrm{Lb}} = -I_{\mathrm{R}}$ is reached. At this point, S2 turns off, and the converter enters a period in which a resonant transition occurs (see Section IV-A). After this, I_{Lb} will flow through the body diode of S1 (see Figure 5), allowing for ZVS turn-on at t_1. The TCM buck converter also achieves ZVS turn-on of S2, in the same way as the regular buck converter.

A. Deadtime Analysis

The process of charging and discharging the output capacitances C_{oss} occurs by means of resonance in the synchronous buck converter. The equivalent circuit during deadtime is shown in Figure 6.

ZVS turn-on of S1 does not occur in a certain range of I_{R}, and whether it is achieved can be determined by numerically solving the equations for a series resonant circuit, given in Section A. By solving these equations it can be seen in

TABLE III: All equations on which the analytical model of the TCM buck converter is based.

| Description	Definition	
Dutycycle	$D = V_{\mathrm{o}}/V_{\mathrm{in}}$	(23)
Switching frequency	$f_{\mathrm{sw}} = \frac{1}{L_{\mathrm{b}}} \cdot D \cdot \frac{V_{\mathrm{in}}-V_{\mathrm{out}}}{2(I_{\mathrm{o}}+I_{\mathrm{R}})}$	(24)
Average Inductor Current	$I_{\mathrm{Lb,avg}} = I_{\mathrm{o}}$	(25)
Peak-to-Peak Inductor Current	$I_{\mathrm{Lb,pk-pk}} = 2(I_{\mathrm{o}} + |I_{\mathrm{R}}|)$	(26)
Maximum Inductor Current	$I_{\mathrm{Lb,max}} = 2(I_{\mathrm{o}} + \frac{1}{2}|I_{\mathrm{R}}|)$	(27)
RMS Inductor Current	$I_{\mathrm{Lb,rms}} = \sqrt{\frac{1}{3}I_{\mathrm{Lb,pk-pk}}^2 - I_{\mathrm{R}}I_{\mathrm{Lb,pk-pk}} + I_{\mathrm{R}}^2}$	(28)
	$k_1 = |I_{\mathrm{R}}|/I_{\mathrm{Lb,pk-pk}}$	(29)
Average high-side switch current	$I_{\mathrm{S1,avg}} = DI_{\mathrm{o}}$	(30)
RMS high-side switch current	$I_{\mathrm{S1,RMS}} = \sqrt{\left(I_{\mathrm{R}}\sqrt{D\frac{k_1}{3}}\right)^2 + \left(I_{\mathrm{Lb,max}}\sqrt{D\frac{1-k_1}{3}}\right)^2}$	(31)
Average low-side switch current	$I_{\mathrm{S2,avg}} = (1 - D)I_{\mathrm{o}}$	(32)
RMS low-side switch current	$I_{\mathrm{S2,RMS}} = \sqrt{\left(I_{\mathrm{R}}\sqrt{(1-D)\frac{k_1}{3}}\right)^2 + \left(I_{\mathrm{Lb,max}}\sqrt{(1-D)\frac{1-k_1}{3}}\right)^2}$	(33)
Turn-off current high-side switch	$I_{\mathrm{S1,off}} = I_{\mathrm{Lb,max}}$	(34)
Turn-off current low-side switch	$I_{\mathrm{S2,off}} = I_{\mathrm{R}}$	(35)
Interleaved output current ripple	$\Delta I_{\mathrm{o}} = \frac{V_{\mathrm{in}}D}{f_{\mathrm{sw}}}\left(1 - \frac{\lfloor N_{\mathrm{phase}}D\rfloor}{N_{\mathrm{phase}}D}\right)\left(1 + \lfloor N_{\mathrm{phase}}D\rfloor - N_{\mathrm{phase}}D\right)$	(36)
Output capacitor RMS current	$I_{\mathrm{Cb,rms}} = \sqrt{\frac{\Delta I_{\mathrm{o}}^2}{12}}$	(37)
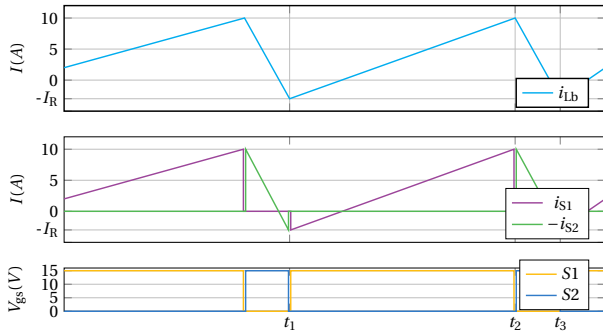
Fig. 4: Operational waveforms of a TCM buck converter, the building block of the second stage in the proposed two-stage converter. i_{Lb} is the current through the inductor of the buck converter, i_{S1} and i_{S2} are the currents through the top and bottom switch of the half bridge, respectively. See Figure 5.
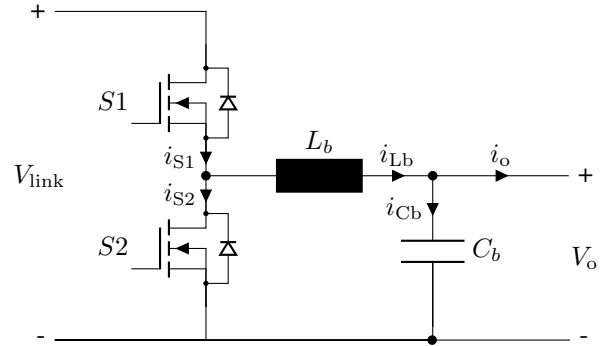

Fig. 5: Schematic of a single TCM buck converter.

Fig. 6: Equivalent circuit of the TCM buck converter during deadtime. This is a series resonant circuit.

Figure 7 that C_{eq} is not always fully charged/discharged for every combination of t_{dead} and I_{R}.

V. CONVERTER DESIGN

A. Design Requirements

The design requirements are listed in Table IV, where the targets for $\Delta I_{\mathrm{o,max}}$, $\Delta V_{\mathrm{o,max}}$ and T_{ambient} are taken from DC charging station standard IEC-61851-23:2014 [23].

B. Semiconductor Selection

LLC converter: Applying the analytical equations from Table II, the maximum average current stress of the switch for the LLC converter can be approximated to be $\hat{I}_{\mathrm{sw,avg}} = 8.59A$.
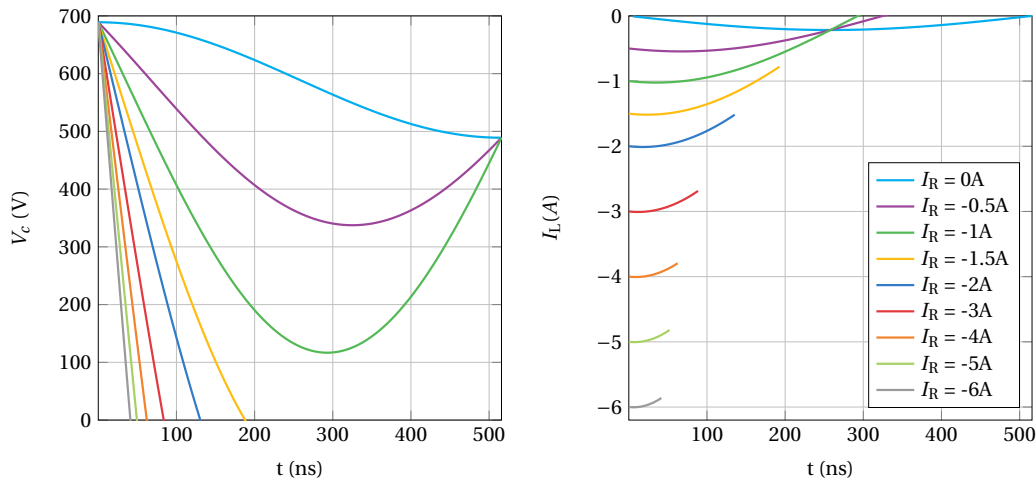
Fig. 7: Voltage across the equivalent capacitance C_{eq} of Figure 6 and the current through the inductor L_{b} at that same time in the resonant interval during t_{dead}. ZVS is only achieved when $V_{\text{c}} = 0\,\text{V}$. This figure shows that not all values of I_{R} will lead to ZVS. V_{in}=689 V, V_{o}=100 V, $C =$355 pF, $L =$75.8 μH.

TABLE IV: Design requirements for the wide output voltage range resonant converter.

Parameter	Symbol	Value
Input voltage range	V_{in}	640-840 V
Output voltage range	V_{out}	150-1000 V
Switching frequency LLC	$f_{\text{sw,LLC}}$	15 kHz
Maximum output power	$P_{\text{o,max}}$	11 kW
Maximum output current	$I_{\text{o,max}}$	30 A
Maximum output current ripple during CC*	$\Delta I_{\text{o,max}}$	9 A
Maximum output voltage ripple during CV*	$\Delta V_{\text{o,max}}$	10 V
Operating temperature range	T_{ambient}	-5-40 °C

And assuming that each switch conducts exactly half of the positive sine wave, the maximum RMS current stress on the switches can be calculated to be $\hat{I}_{\text{sw,rms}} = 13.5A$.

A range of different 1200 V commercial MOSFET and IGBT devices that suit these requirements are compared. The switches that would result in the lowest losses for the LLC converter are selected:

- LLC IGBT version: IKW40N120CS6 from Infineon.
- LLC MOSFET version: IMW120R060M1 from Infineon.

Interleaved TCM buck converter: The maximum output current is $I_{\text{o,max}} = 30\,\text{A}$. Since $N_{\text{phase}} \geq 2$, the average output current of a single buck converter is, therefore, maximum 15 A. Taking the conservative values of $I_R = -5\,\text{A}$ and $D = 1$, the maximum current stress of the interleaved TCM buck converter switch can be calculated using (26), (29) and (31) to be $I_{\text{S1,rms}} = 18.93A$.

The requirements for the switches in the Interleaved TCM buck converter in Configuration One are equal to the requirements for the switches of the LLC converter. Therefore the same two switches are selected: as IGBT the IKW40N120CS6 and as MOSFET the IMW120R060M1.

C. Resonant Capacitors

The resonant capacitors in the LLC converter are subject to the total transformer current. The maximum voltage amplitude across the capacitor is calculated using (11). The maximum $I_{\text{Lr,rms}}$ follows from the design script and is equal to 20 Arms. The capacitor bank is arranged with N_{p} parallel capacitors to lower the RMS current on an individual capacitor. The selected resonant capacitor is the B32671L6473K000: (47 nF). These capacitors have a DC voltage rating of 630 V, with no derating required at f_{sw}=15 kHz. The required voltage rating, using (11), is only ≈200 V (peak). The number of parallel capacitors to achieve the required C_{r} is 33.

D. Transformer Design

The operating frequency of the LLC converter is relatively low ($f_{\text{sw,LLC}}=$ 15 kHz), as stated in Table IV. This low frequency and high power naturally results in the requirement of large area-product cores. The minimal number of turns of the primary side winding can be calculated by (38).

$$N_{\text{min}} = \frac{V_{\text{in}}}{4 \cdot A_{\text{c}} \cdot B_{\text{op}} \cdot f_{\text{sw}}} \tag{38}$$

An airgap might be required to lower the magnetizing inductance value L_{m}, required to satisfy ZVS requirements of the LLC converter. The relationship between the airgap length and the magnetizing inductance can be approximated by (39).

$$L \approx \frac{N^2}{R_{\text{g}}} \approx \frac{N^2}{2 \cdot l_{\text{air}}/\mu_0 A_{\text{c}}} \tag{39}$$

The winding losses are calculated in MATLAB based on the procedure described by Mühlethaler et al. (2012) [24], and the core losses are calculated using the improved Generalized Steinmetz Equation (iGSE) [24] [68]. The details are not further elaborated upon in this work.

TABLE V: All components in the final design of the LLC converter.

Component	Description/Part Number
LLC IGBT's	IKW40N120CS6
Resonant capacitors	B32671L6473K000 (47 nF)
Transformer core shape	EE70/33/32
Number of parallel cores n_{cores}	5
Transformer Airgap	0.3 mm
N_{pri}	20
N_{sec}	30 (2 · 15)
Magnetizing Inductance L_{m}	4.8 mH
External Resonant Inductor Core Shape	EE70/33/32
Number of parallel cores n_{cores}	1
Inductor airgap	1.3 mm
N	14
Resonant Inductance L_{r}	64.43 uH
Rectifier Diodes	IDW30G120C5B
LLC output capacitors	C4AQIBW5600A3NJ (2 · 2·60 uF)

TABLE VI: All components in the final design of the Interleaved TCM buck converter.

Component	Description/Part Number
SiC MOFSET's	IMW120R060M1 (2 · 2 · 2)
Parallel phases per module N_{phase}	2
Inductor core shape	EE70/33/32
Number of parallel cores n_{cores}	1
Inductor airgap	1.6 mm
N	12
buck Inductance L_{b}	75.6 uH
LLC output capacitors	C4AQILW5150A36J (2 · 2·15 uF
Power Relays	TE-T9G (3x)

E. Inductor Design

The work in [15] is used for designing the four inductors of the Interleaved TCM buck converter and the external resonant inductor $L_{\text{r,ext}}$ of the LLC converter. The minimum number of turns can be calculated using (40), and the required airgap length l_{g} to achieve the required inductance can be calculated by (41).

$$N_{\min} = \frac{L I_{\max}}{B_{\max} A_{\text{c}}} \tag{40}$$

$$l_{\text{g}} = \frac{L I_{\max}^2 \mu_0}{B_{\max}^2 A_{\text{c}}} \tag{41}$$

The winding losses and core loss are, again, calculated in MATLAB based on the procedure described in [24] [68].

F. Design Summary

The selection choices of all other components of the proposed converter are summarized in Tables V and VI. The output capacitors of the Interleaved TCM buck converter are selected to meet the requirements from IEC-61851-23:2014 [23] (see Table IV).

VI. RESULTS OF THE ANALYTICAL COMPARISON

In order to compare the efficiency performance of the two possible configurations presented in Figure 1, the charging-cycle efficiency [15] is used, which represents the average efficiency of the converter over the whole charging process.

As explained in Section II, two possible configurations of the two-stage converter were compared together with the use of either SiC MOSFETs or IGBTs. The results for the first stage, the LLC converter, are given in Section VI-A, while the results of the Interleaved TCM buck converter configuration comparison are given in Section VI-B.

A. LLC converter

For the LLC converter in this paper only a comparison was made between a SiC MOSFET based or IGBT based LLC converter. The performance of the converter was measured based on the charging cycle efficiencies, as explained in [15]. Table VII indicates that the efficiency of both the SiC MOSFET based and IGBT based LLC converter have approximately the same charging cycle efficiencies, given $f_{\text{sw}} = 15$ kHz. Therefore, the IKW40N120CS6 IGBT version of the LLC converter is selected due to its lower cost.

TABLE VII: Efficiency and Losses of the 11 kW LLC converter using either a MOSFET (IMW120R060M1) or an IGBT (IKW40N120CS6) as transistor (V_{in} =840 V).

Switch Type	Charge Cycle Efficiencies ($\eta(-)$)				
	11 kW 400 V	55 kW 400 V	11 kW 800 V	55 kW 800 V	Average
IMW120R060M1	0.9799	0.9787	0.9798	0.9795	**0.9795**
IKW40N120CS6	0.9796	0.9763	0.9795	0.9786	**0.9784**

B. Interleaved TCM buck converter

The comparison of different design solutions for the Interleaved TCM buck converter is more elaborate because a given design solution consists of 5 different variables:

- Configuration 1 or 2
- Minimum switching frequency (see (24))
- IGBT or SiC MOSFET based
- Number of interleaved phases per module N_{phase}

Running the analytical comparison of several possible design solutions and comparing the average efficiency of all four charging cycles proposed in [15] gives us the solution space given in Figure 8. Note that no competitive IGBT could be found for use in Configuration 2 (which requires higher $V_{\text{DS,max}}$ than Configuration 1) due to the unsatisfactory switching losses performance from the devices available on the market.

It can be seen that the MOSFET-based solutions are more efficient when compared to IGBT-based solutions. And, specifically, Configuration 1 using MOSFETs generates the most
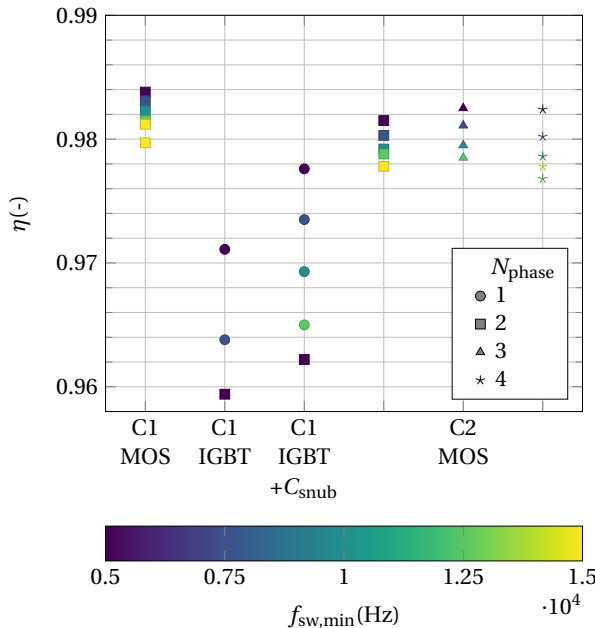
Fig. 8: Average charging cycle efficiency of the Interleaved TCM buck converter solution space. C1 = Configuration 1, and C2 = Configuration 2.
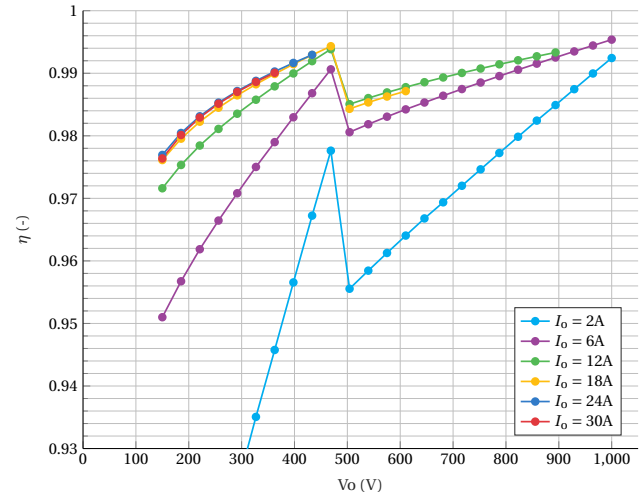

Fig. 9: Analytical efficiency of the TCM buck converter for different I_o over the entire V_o range (with $V_{in} = 525\,\mathrm{V}$).

efficient converters for each respective $f_{sw,min}$. The selected solution for the TCM buck converter in this paper is shown in Table VIII.

TABLE VIII: Selected final design of the TCM buck converter in this paper.

Design Parameter	Value
Configuration	1
$f_{sw,min}$	15 kHz
Switch technology	MOSFET
Switches	IMW120R060M1
N_{phase}	2

The reason that IGBT-based converters achieve a lower average efficiency in the TCM buck converter is because of the high switching frequencies operation required for partial loads (see (24)).

The calculated efficiency of the selected design solution of the Interleaved TCM buck converter over the entire operating range of the system is shown next to the measured efficiency in Figure 9.

VII. COMPARISON TO CONVENTIONAL FREQUENCY-MODULATED LLC

In order to emphasize the benefit of the proposed two-stage wide output voltage range EV charger solution, a comparison is made with the conventional frequency-modulated LLC converter. To do this, the buck stage is removed from the two-stage converter shown in Figure 1b, however, the re-configurable secondary sides of the LLC are kept to improve efficiency and

reduce switching frequency operational range. The proposed LLC design from Table V is then employed using solely pulse frequency modulation to control the output voltage (rLLC PFM). The analytical efficiency comparison over the entire operational range is shown in Figure 10.
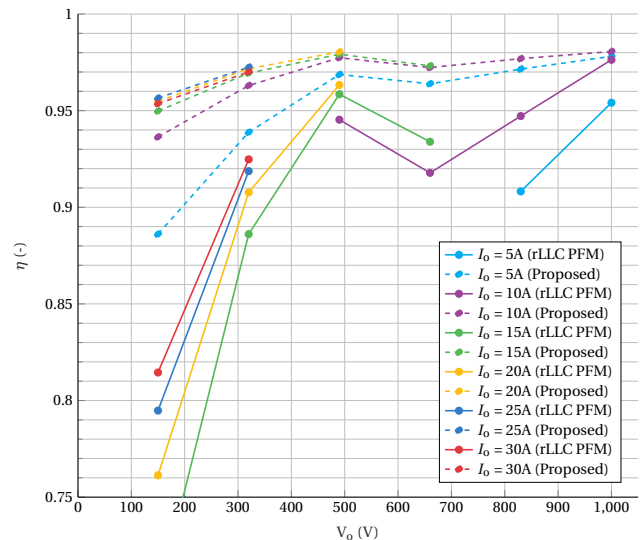

Fig. 10: Analytical efficiency comparison between the proposed solution and the conventional frequency modulated LLC converter (rLLC PFM). The output voltage is on the x-axis, and the colors indicate different I_o.

Judging from Figure 10, the benefit of the proposed wide output voltage EV charger appears evidently: the proposed solution is highly efficient over the entire operational range, which is not the case for the rLLC PFM. The switching frequency operational range of the rLLC PFM is 4.8-87.3kHz. Operational points which showed large deviations between the analytical model and LTSpice simulations are not displayed for the rLLC PFM. These were operational points for which the FHA model was not valid. The rLLC PFM deviates from the series resonant frequency operational point, which creates

reactive currents in the RTN that cause additional losses. On top of that, the IGBTs need to switch at multiples of the base $15\,\mathrm{kHz}$ for some operational points, causing additional switching losses.

This almost flat high-efficiency curve of the proposed solution is enabled due to the unique combination of the LLC converter, Interleaved TCM Buck converter and re-configurable stage, resulting in the highest reported output voltage range for a resonant converter based EV charger while maintaining this almost flat high-efficiency curve.

VIII. EXPERIMENTAL RESULTS

The selected design solutions for the LLC converter and Interleaved TCM buck converter are verified experimentally. Figures 11 and 12 present the hardware demonstrators of the LLC converter and Interleaved TCM buck converter, respectively.
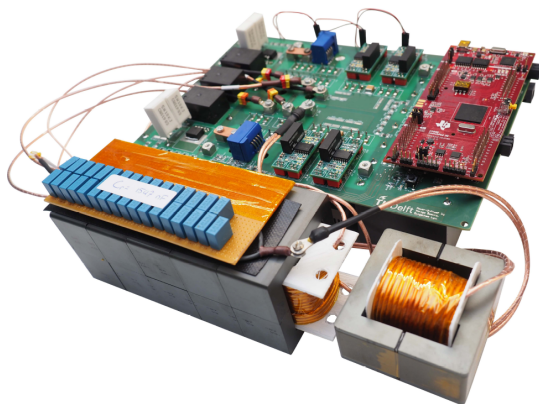
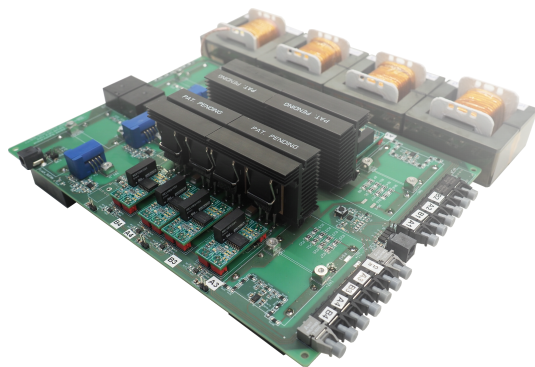Fig. 11: Designed LLC converter hardware demonstrator.

Fig. 12: Designed interleaved TCM buck converter hardware demonstrator.

A. LLC converter

The experimentally measured efficiency of the LLC converter over the load range from $400\,\mathrm{W}$ to $11\,\mathrm{kW}$ with an input voltage of $640\,\mathrm{V}$ is shown in Figure 13. The peak efficiency of the LLC converter is 98.231% at $P_\mathrm{o} = 6.37\,\mathrm{kW}$; see Figure 14.

The measured operational waveforms at different output powers of the LLC converter are shown in Figure 15.
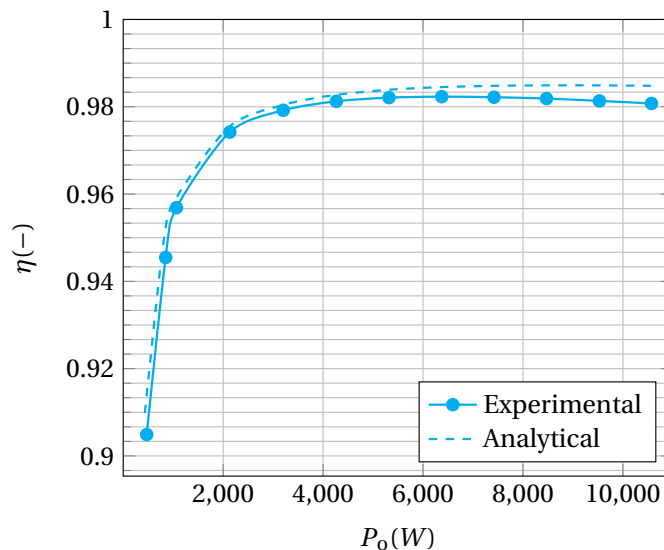

Fig. 13: LLC converter efficiency over the entire output power range P_o as calculated analytically and measured experimentally.
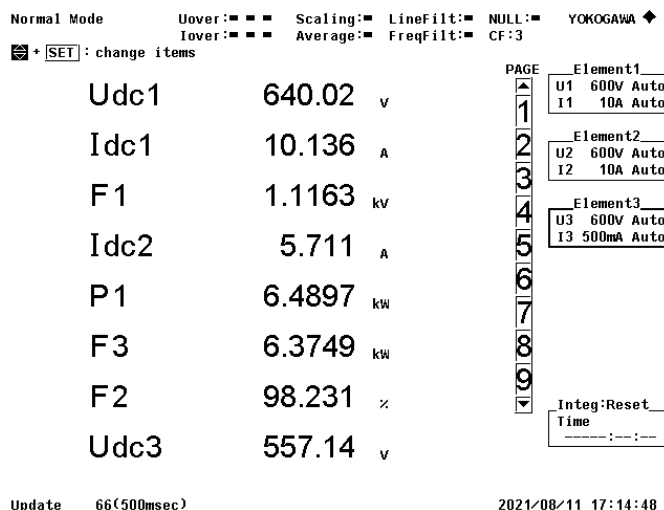

Fig. 14: Screenshot taken on the Yokogawa WT500 Power Analyzer at the operation point with the highest measured efficiency P_o=6.37 kW.

B. Interleaved TCM buck converter

The efficiency of the selected interleaved TCM buck converter solution presented in Table VIII is measured. The results are given in Figure 16, where they are compared with the calculated efficiency. The peak efficiency is measured at V_o=1000 V and I_o=5 A at 99.577%.

The waveforms of the Interleaved TCM buck converter at different operating points are given in Figures 18 and 19. The converter is placed in Current-Doubler mode in Figure 18, and in Voltage-Doubler mode in Figure 19Note that, the data shown for the voltage-doubler mode is measured only in one of the interleaved TCM buck converters.
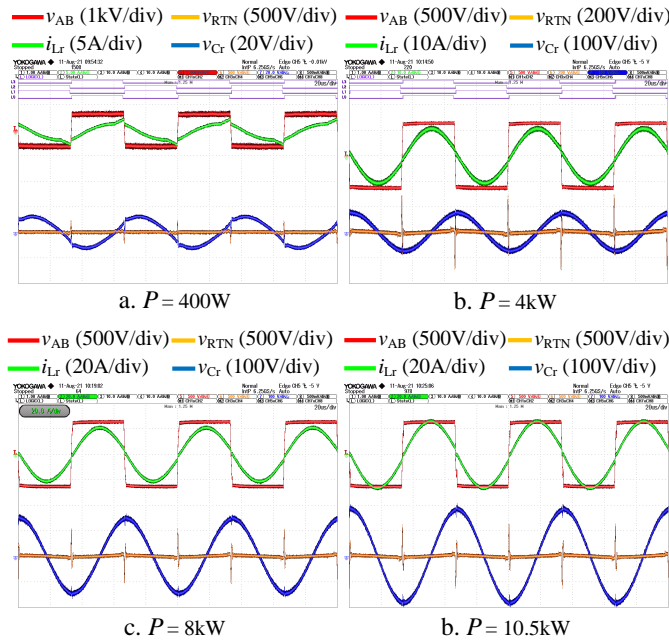
Fig. 15: The operational waveforms of the LLC converter at different output powers P_o, with V_in=640V. i_Lr is the current through the resonant inductor, v_Cr is the voltage across the resonant capacitor, v_AB and v_RTN are the terminal voltage from the H-bridge and the voltage across the resonant tank network (the voltage across the series connection of L_r and C_r), respectively.
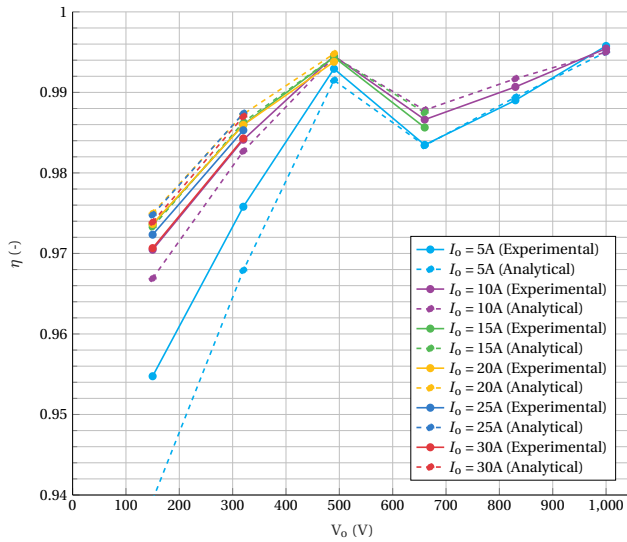

Fig. 16: Comparison of $\eta_\mathrm{analytical}$ and η_measured for the Interleaved TCM Buck converter over the entire operating range. The output voltage is on the x-axis, and the colors indicate different I_o.

C. Two-stage converter efficiency

The power efficiencies of the two individual stages were given in the previous sections, Sections VIII-A and VIII-B. Combining the power efficiencies given in these sections gives the total efficiency of the proposed two-stage converter in
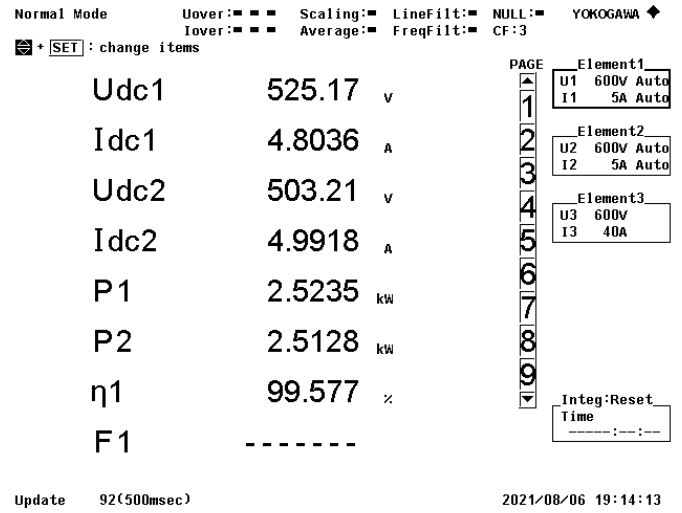

Fig. 17: A screenshot taken on the Yokogawa WT500 Power Analyzer at the operation point with the highest measured efficiency V_o=1000 V, I_o=5 A.
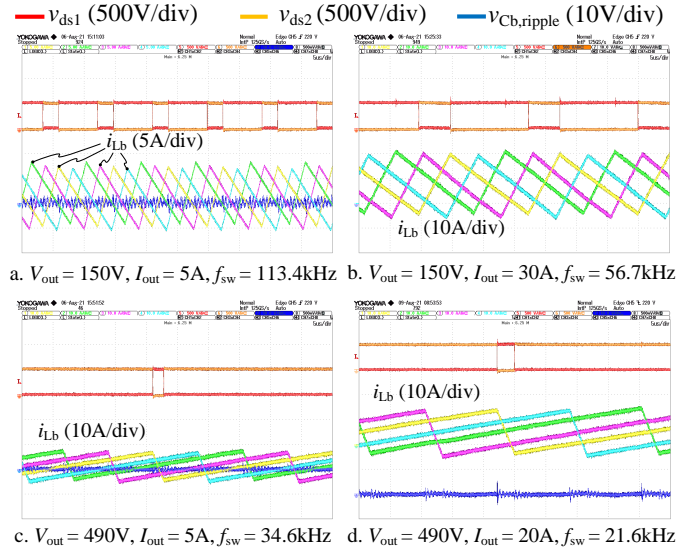

Fig. 18: The operational waveform of the Interleaved TCM buck converter in current-doubler mode in different output voltage and current, with V_in=525V. v_ds1 is the drain-source voltage on the high-side MOSFET, v_ds2 is the drain-source voltage on the low-side MOSFET, $v_\mathrm{Cb,ripple}$ is the voltage ripple on the output capacitor C_b.

Figure 20, achieving a peak efficiency of 97.66%.

IX. CONCLUSION

The aim of the current study was to propose an $11\,\mathrm{kW}$ DC-DC converter that is suited for EV charging with a wide output voltage range with very high efficiency over the entire operational range based on a resonant power converter topology. The implemented solution consisted of a two-stage power converter. This is based on an LLC resonant converter followed by an Interleaved TCM buck converter. The achieved output voltage range of 150-1000 V in the current study was
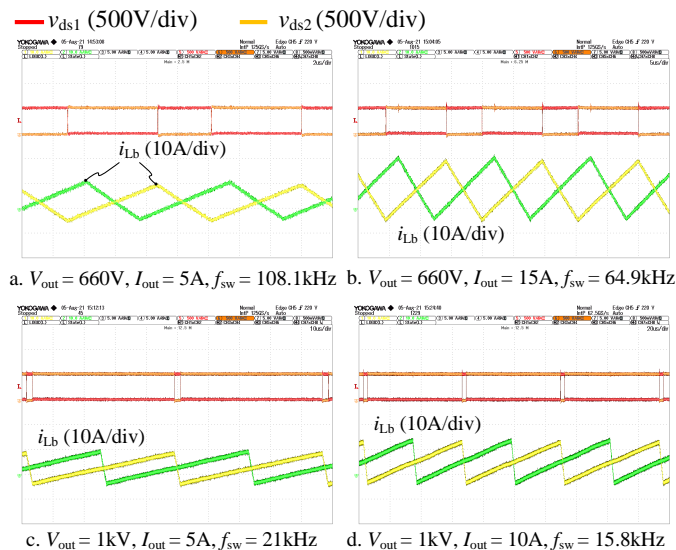
a. V_{out} = 660V, I_{out} = 5A, f_{sw} = 108.1kHz b. V_{out} = 660V, I_{out} = 15A, f_{sw} = 64.9kHz

c. V_{out} = 1kV, I_{out} = 5A, f_{sw} = 21kHz d. V_{out} = 1kV, I_{out} = 10A, f_{sw} = 15.8kHz

Fig. 19: The operational waveform of the Interleaved TCM buck converters in voltage-doubler mode in different output voltage and current, with V_{in}=525V. v_{ds1} is the drain-source voltage on the high-side MOSFET, v_{ds2} is the drain-source voltage on the low-side MOSFET.
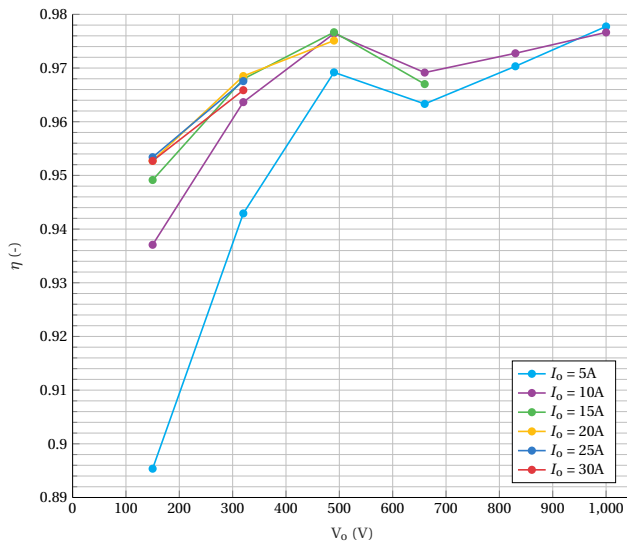

Fig. 20: Measured efficiency of the two-stage LLC + interleaved TCM buck converter over the entire operating range. The efficiencies of the Interleaved TCM buck converter in Figure 16 are multiplied by the (interpolated) efficiency of the LLC converter determined from Figure 13 to obtain the efficiency of the two-stage converter.

not previously reported in literature regarding resonant power converters for EV charging. And therefore, the proposed converter is capable of charging different EV battery types while doing so very efficiently. A prototype of the proposed converter was designed and used to evaluate the efficiency: >95% efficiency was achieved over the entire output voltage range at maximum power, with a peak efficiency of 97.66%. The obtained efficiency for the $11\,\text{kW}$-$400\,\text{V}$ Charging cycle

is 96.85% and 95.67% for the $11\,\text{kW}$-$800\,\text{V}$ Charging cycle.

APPENDIX A
SERIES RESONANT CIRCUIT

Applying KVL and KCL to the equivalent circuit results in the differential equations for $V_{\text{C,eq}}(t)$ and $I_{\text{Lb}}(t)$.

$$
\begin{aligned}
V_{\text{C,eq}}(t) &= (V_{\text{in}} - V_{\text{o}}) - ((V_{\text{in}} - V_{\text{o}}) - V_{\text{c0}})\cos(t - t_0) \\
&\quad + Z_0 \cdot I_{\text{L0}}\sin(\omega_0(t - t_0)) \\
&= (V_{\text{in}} - V_{\text{o}}) + V_{\text{o}}\cos(t - t_0) \\
&\quad + Z_0 \cdot I_{\text{L0}}\sin(\omega_0(t - t_0)) \quad (42)
\end{aligned}
$$

$$
I_{\text{Lb}}(t) = (V_{\text{in}} - V_{\text{o}}) + Z_0 \cdot I_{\text{L0}} \cdot \sin(w_0 \cdot t_{\text{dead}}) \quad (43)
$$

REFERENCES

[1] *Paris Agreement (English)*. United Nations. [Online]. Available: https://unfccc.int/documents/37107

[2] *Global EV Outlook 2021 - Accelerating ambitions despite the pandemic*. International Energy Agency (IEA). [Online]. Available: https://iea.blob.core.windows.net/assets/ed5f4484-f556-4110-8c5c-4ede8bcba637/GlobalEVOutlook2021.pdf

[3] *Powertrain Efficiency: Sustaining EV Growth in an Era of Shortages, Reports IDTechEx*. Bloomberg. [Online]. Available:https://www.bloomberg.com/press-releases/2022-08-03/powertrain-efficiency-sustaining-ev-growth-in-an-era-of-shortages-reports-idtechex

[4] A. Mohsen, N. Mithulananthan and R. Sharma, "A review on topologies for fast charging stations for electric vehicles," in *Proc. 2016 International IEEE Power System Technology (POWERCON)*, Wollongong, NSW, Australia, 2016, pp. 1–6. DOI: 10.1109/POWERCON.2016.7753886.

[5] H. Wang, S. Dusmez and A. Khaligh, "A novel approach to design EV battery chargers using SEPIC PFC stage and optimal operating point tracking technique for LLC converter," in *2014 IEEE Applied Power Electronics Conference and Exposition - APEC 2014)*, Fort Worth, TX, USA, 2014, pp. 1683–1689. DOI: 10.1109/APEC.2014.6803532.

[6] C. Shi, H. Wang, S. Dusmez and A. Khaligh, "A SiC-Based High-Efficiency Isolated Onboard PEV Charger With Ultrawide DC-Link Voltage Range," *IEEE Transactions on Industry Applications*, vol. 53, pp. 501–511, 2017. DOI: 10.1109/TIA.2016.2605063.

[7] C. Wei, D. Zhu, H. Xie, Y. Liu and J. Shao, "A SiC-Based 22kW Bidirectional CLLC Resonant Converter with Flexible Voltage Gain Control Scheme for EV On-Board Charger," in *PCIM Europe digital days 2020; International Exhibition and Conference for Power Electronics, Intelligent Motion, Renewable Energy and Energy Management*, Germany, 2020, pp. 1–7.

[8] Y. Xuan, x. Yang, W. Chen, T. Liu and X. Hao, "A Novel Three-level CLLC Resonant DC-DC Converter for Bidirectional EV Charger in DC Microgrids," *IEEE Transactions on Industrial Electronics*, vol. 68, pp. 2334–2344, 2021. DOI: 10.1109/TIE.2020.2972446.

[9] B. Xue, H. Wang, J. Liang, Q. Cao and Z. Li, "Phase-Shift Modulated Interleaved LLC Converter With Ultrawide Output Voltage Range," *IEEE Transactions on Power Electronics*, vol. 36, pp. 1941–0107, 2021. DOI: 10.1109/TPEL.2020.3001126.

[10] M. Imran Shahzad, S. Iqbal and S. Taib, "Interleaved LLC Converter With Cascaded Voltage-Doubler Rectifiers for Deeply Depleted PEV Battery Charging," *IEEE Transactions on Transportation Electrification*, vol. 4, pp. 89–98, 2018. DOI: 10.1109/TTE.2017.2753407.

[11] W.-S. Lee, J. Kim, J. Lee and I. Lee, "Design of an Isolated DC/DC Topology With High Efficiency of Over 97% for EV Fast Chargers," *IEEE Transactions on Vehicular Technology*, vol. 68, pp. 11725-11737, 2019. DOI: 10.1109/TVT.2019.2949080.

[12] Y. Wei, Q. Luo and A. Mantooth, "Overview of Modulation Strategies for LLC Resonant Converter," *IEEE Transactions on Power Electronics*, vol. 35, pp. 10423-10443, 2020. DOI: 10.1109/TPEL.2020.2975392.

[13] M. Kwon, S. Jung and S. Choi, "A high efficiency bi-directional EV charger with seamless mode transfer for V2G and V2H application," in *2015 IEEE Energy Conversion Congress and Exposition (ECCE)*, Montreal, QC, Canada, 2015, pp. 5394–5399. DOI: 10.1109/ECCE.2015.7310418.

[14] Z. U. Zahid, Z. M. Dalala, R. Chen, B. Chen and J. Lai, "Design of Bidirectional DC–DC Resonant Converter for Vehicle-to-Grid (V2G) Applications," *IEEE Transactions on Transportation Electrification*, vol. 1, pp. 232–244, 2015. DOI: 10.1109/TTE.2015.2476035.

[15] D. Lyu, T. Batista Soeiro and P. Bauer, "Design and Implementation of a Re-configurable Phase-Shift Full-Bridge Converter for Wide Voltage Range EV Charging Application," *IEEE Transactions on Transportation Electrification (Early Access)*, DOI: 10.1109/TTE.2022.3176826.

[16] Y. -C. Liu, Y. -L. Syu, N. A. Dung, C. Chen, K. -D. Chen and K. A. Kim, "High-Switching-Frequency TCM Digital Control for Bidirectional-Interleaved buck Converters Without Phase Error for Battery Charging," in *IEEE Journal of Emerging and Selected Topics in Power Electronics*, vol. 8, no. 3, pp. 2111-2123, Sept. 2020, DOI: 10.1109/JESTPE.2019.2954602.

[17] C. -S. Yeh, X. Zhao and J. -S. Lai, "An investigation on zero-voltage-switching condition in synchronous-conduction-mode buck converter," *2017 IEEE Energy Conversion Congress and Exposition (ECCE)*, 2017, pp. 1728-1732, DOI: 10.1109/ECCE.2017.8096002.

[18] D. Christen, S. Tschannen and J. Biela, "Highly efficient and compact DC-DC converter for ultra-fast charging of electric vehicles," *2012 15th International Power Electronics and Motion Control Conference (EPE/PEMC)*, 2012, pp. LS5d.3-1-LS5d.3-8, DOI: 10.1109/EPEPEMC.2012.6397481.

[19] *Benefits of a multiphase buck converter*. Texas Instruments Inc. [Online]. Available: https://www.ti.com/lit/an/slyt449/slyt449.pdf

[20] R. L. Steigerwald, "A comparison of half-bridge resonant converter topologies," in *IEEE Transactions on Power Electronics*, vol. 3, no. 2, pp. 174-182, April 1988, DOI: 10.1109/63.4347.

[21] U. Kundu, K. Yenduri and P. Sensarma, "Accurate ZVS Analysis for Magnetic Design and Efficiency Improvement of Full-Bridge LLC Resonant Converter," in *IEEE Transactions on Power Electronics*, vol. 32, no. 3, pp. 1703-1706, March 2017, DOI: 10.1109/TPEL.2016.2604118.

[22] M. Kasper, R. M. Burkart, G. Deboy and J. W. Kolar, "ZVS of Power MOSFETs Revisited," in *IEEE Transactions on Power Electronics*, vol. 31, no. 12, pp. 8063-8067, Dec. 2016, DOI: 10.1109/TPEL.2016.2574998.

[23] *Electric vehicle conductive charging system - Part 23: DC electric vehicle charging station*, IEC61851-23:2014, International Electrotechnical Commission, Geneva, CH, 2014.

[24] J. Mühlethaler, "Modeling and multi-objective optimization of inductive power components," Doctoral Dissertation, Dep. Inf.technologie und Elektrotechnik, ETH Zurich, Zurich, Switzerland, 2012. DOI: 10.3929/ethz-a-007328104

[25] C. Jung, "Power Up with 800-V Systems: The benefits of upgrading voltage power for battery-electric passenger vehicles," in *IEEE Electrification Magazine*, vol. 5, no. 1, pp. 53-58, March 2017, DOI: 10.1109/MELE.2016.2644560.

[26] T. B. Soeiro, J. Mühlethaler, J. Linnér, P. Ranstad and J. W. Kolar, "Automated Design of a High-Power High-Frequency LCC Resonant Converter for Electrostatic Precipitators," in *IEEE Transactions on Industrial Electronics*, vol. 60, no. 11, pp. 4805-4819, Nov. 2013, DOI: 10.1109/TIE.2012.2227897.

[27] R. Gadelrab, Y. Yang, B. Li, F. Lee and Q. Li, "High-Frequency High-Density Bidirectional EV Charger," *2018 IEEE Transportation Electrification Conference and Expo (ITEC)*, 2018, pp. 687-694, DOI: 10.1109/ITEC.2018.8450117.

[28] B. Li, Q. Li and F. C. Lee, "A WBG based three phase 12.5 kW 500 kHz CLLC resonant converter with integrated PCB winding transformer," *2018 IEEE Applied Power Electronics Conference and Exposition (APEC)*, 2018, pp. 469-475, DOI: 10.1109/APEC.2018.8341053.

[29] L. A. D. Ta, N. D. Dao and D. Lee, "High-Efficiency Hybrid LLC Resonant Converter for On-Board Chargers of Plug-In Electric Vehicles," in *IEEE Transactions on Power Electronics*, vol. 35, no. 8, pp. 8324-8334, Aug. 2020, DOI: 10.1109/TPEL.2020.2968084.

[30] Shen, C., Xiao, Q. and Zhang, Y. (2020), High-efficiency design method of LLC resonant converter for PHEV battery chargers (based on time-domain model). *IET Electr. Syst. Transp.*, 10: 234-242. DOI: 10.1049/iet-est.2019.0092.

[31] H. Wang and Z. Li, "A PWM LLC Type Resonant Converter Adapted to Wide Output Range in PEV Charging Applications," in *IEEE Transactions on Power Electronics*, vol. 33, no. 5, pp. 3791-3801, May 2018, DOI: 10.1109/TPEL.2017.2713815.

[32] Y. Shen, W. Zhao, Z. Chen and C. Cai, "Full-Bridge LLC Resonant Converter With Series-Parallel Connected Transformers for Electric Vehicle On-Board Charger," in *IEEE Access*, vol. 6, pp. 13490-13500, 2018, DOI: 10.1109/ACCESS.2018.2811760.

[33] H. Vu and W. Choi, "A Novel Dual Full-Bridge LLC Resonant Converter for CC and CV Charges of Batteries for Electric Vehicles," in *IEEE Transactions on Industrial Electronics*, vol. 65, no. 3, pp. 2212-2225, March 2018, DOI: 10.1109/TIE.2017.2739705.

[34] H. Li et al., "A 6.6kW SiC bidirectional on-board charger," *2018 IEEE Applied Power Electronics Conference and Exposition (APEC)*, 2018, pp. 1171-1178, DOI: 10.1109/APEC.2018.8341164.

[35] N. Shafiei, M. Ordonez, M. Craciun, C. Botting and M. Edington, "Burst Mode Elimination in High-Power LLC Resonant Battery Charger for Electric Vehicles," in *IEEE Transactions on Power Electronics*, vol. 31, no. 2, pp. 1173-1188, Feb. 2016, DOI: 10.1109/TPEL.2015.2420573.

[36] I. Lee, "Hybrid PWM-Resonant Converter for Electric Vehicle On-Board Battery Chargers," in *IEEE Transactions on Power Electronics*, vol. 31, no. 5, pp. 3639-3649, May 2016, DOI: 10.1109/TPEL.2015.2456635.

[37] H. Haga and F. Kurokawa, "A novel modulation method of the full bridge three-level LLC resonant converter for battery charger of electrical vehicles," *2015 IEEE Energy Conversion Congress and Exposition (ECCE)*, 2015, pp. 5498-5504, DOI: 10.1109/ECCE.2015.7310433.

[38] J. Deng, S. Li, S. Hu, C. C. Mi and R. Ma, "Design Methodology of LLC Resonant Converters for Electric Vehicle Battery Chargers," in *IEEE Transactions on Vehicular Technology*, vol. 63, no. 4, pp. 1581-1592, May 2014, DOI: 10.1109/TVT.2013.2287379.

[39] H. Wang, S. Dusmez and A. Khaligh, "A novel approach to design EV battery chargers using SEPIC PFC stage and optimal operating point tracking technique for LLC converter," *2014 IEEE Applied Power Electronics Conference and Exposition - APEC 2014*, 2014, pp. 1683-1689, DOI: 10.1109/APEC.2014.6803532.

[40] K. Colak, E. Asa, M. Bojarski and D. Czarkowski, "Hybrid control approach of CLL resonant converter for EV battery chargers," *IECON 2014 - 40th Annual Conference of the IEEE Industrial Electronics Society*, 2014, pp. 5041-5046, DOI: 10.1109/IECON.2014.7049266.

[41] J. Deng, S. Li, S. Hu, C. C. Mi and R. Ma, "Design Methodology of LLC Resonant Converters for Electric Vehicle Battery Chargers," in *IEEE Transactions on Vehicular Technology*, vol. 63, no. 4, pp. 1581-1592, May 2014, DOI: 10.1109/TVT.2013.2287379.

[42] J. Lee and H. Chae, "6.6-kW Onboard Charger Design Using DCM PFC Converter With Harmonic Modulation Technique and Two-Stage DC/DC Converter," in *IEEE Transactions on Industrial Electronics*, vol. 61, no. 3, pp. 1243-1252, March 2014, DOI: 10.1109/TIE.2013.2262749.

[43] N. D. Dao, D. Lee and Q. D. Phan, "High-Efficiency SiC-Based Isolated Three-Port DC/DC Converters for Hybrid Charging Stations," in *IEEE Transactions on Power Electronics*, vol. 35, no. 10, pp. 10455-10465, Oct. 2020, DOI: 10.1109/TPEL.2020.2975124.

[44] B. Lee, J. Kim, S. Kim and J. Lee, "A PWM SRT DC/DC Converter for 6.6-kW EV Onboard Charger," in *IEEE Transactions on Industrial Electronics*, vol. 63, no. 2, pp. 894-902, Feb. 2016, DOI: 10.1109/TIE.2015.2480384.

[45] Y. Kim and J. Lee, "Full-Bridge+SRT Hybrid DC/DC Converter for a 6.6-kW EV On-Board Charger," in *IEEE Transactions on Vehicular Technology*, vol. 65, no. 6, pp. 4419-4428, June 2016, DOI: 10.1109/TVT.2016.2535237.

[46] Park, J., Kim, M. and Choi, S. (2014), "Zero-current switching series loaded resonant converter insensitive to resonant component tolerance for battery charger," *IET Power Electronics*, 7: 2517-2524. DOI: 10.1049/iet-pel.2013.0757.

[47] Z. Li, X. Yang, Y. Li, J. Li, B. Zhang and T. Lei, "Design and Implementation of a High-efficiency DC/DC Converter for EVs Charging Basing on LLC Resonant Topology and Silicon-Carbide Devices," *2018 IEEE International Power Electronics and Application Conference and Exposition (PEAC)*, 2018, pp. 1-6, DOI: 10.1109/PEAC.2018.8590636.

[48] S. A. Arshadi, M. Ordonez, W. Eberle, M. Craciun and C. Botting, "Three-Phase LLC Battery Charger: Wide Regulation and Improved Light-Load Operation," in *IEEE Transactions on Power Electronics*, vol. 36, no. 2, pp. 1519-1531, Feb. 2021, DOI: 10.1109/TPEL.2020.3006422.

[49] H. Wang, M. Shang and D. Shu, "Design Considerations of Efficiency Enhanced LLC PEV Charger Using Reconfigurable Transformer," in *IEEE Transactions on Vehicular Technology*, vol. 68, no. 9, pp. 8642-8651, Sept. 2019, DOI: 10.1109/TVT.2019.2930551.

[50] B. Lee, J. Kim, S. Kim and J. Lee, "An Isolated/Bidirectional PWM Resonant Converter for V2G(H) EV On-Board Charger," in *IEEE Transactions on Vehicular Technology*, vol. 66, no. 9, pp. 7741-7750, Sept. 2017, DOI: 10.1109/TVT.2017.2678532.

[51] Zhang, Z. and Khaligh, A. (2020), Modelling and optimisation of a dual-control MHz-level CLLC converter with minimised power losses in battery charging applications. *IET Power Electronics*, 13: 1575-1582. DOI: 10.1049/iet-pel.2019.1221

[52] Z. Zhang, C. Liu, M. Wang, Y. Si, Y. Liu and Q. Lei, "High-Efficiency High-Power-Density CLLC Resonant Converter With Low-Stray-Capacitance and Well-Heat-Dissipated Planar Transformer for EV On-Board Charger," in *IEEE Transactions on Power Electronics*, vol. 35, no. 10, pp. 10831-10851, Oct. 2020, DOI: 10.1109/TPEL.2020.2980313.

[53] A. M. Ammar, K. Ali and D. J. Rogers, "A Bidirectional GaN-Based CLLC Converter for Plug-In Electric Vehicles On-Board Chargers," *IECON 2020 The 46th Annual Conference of the IEEE Industrial Electronics Society*, 2020, pp. 1129-1135, DOI: 10.1109/IECON43393.2020.9254560.

[54] H. -T. Chang, T. -J. Liang and W. -C. Yang, "Design and Implementation of Bidirectional DC-DC CLLLC Resonant Converter," *2018 IEEE Energy Conversion Congress and Exposition (ECCE)*, 2018, pp. 2712-2719, DOI: 10.1109/ECCE.2018.8557697

[55] G. Liu, D. Li, J. Q. Zhang, B. Hu and M. L. Jia, "Bidirectional CLLC resonant DC-DC converter with integrated magnetic for OBCM application," *2015 IEEE International Conference on Industrial Technology (ICIT)*, 2015, pp. 946-951, DOI: 10.1109/ICIT.2015.7125219.

[56] H. Wang, S. Dusmez and A. Khaligh, "Design and Analysis of a Full-Bridge LLC-Based PEV Charger Optimized for Wide Battery Voltage Range," in *IEEE Transactions on Vehicular Technology*, vol. 63, no. 4, pp. 1603-1613, May 2014, DOI: 10.1109/TVT.2013.2288772.

[57] G. Liu, Y. Jang, M. M. Jovanović and J. Q. Zhang, "Implementation of a 3.3-kW DC–DC Converter for EV On-Board Charger Employing the Series-Resonant Converter With Reduced-Frequency-Range Control," in *IEEE Transactions on Power Electronics*, vol. 32, no. 6, pp. 4168-4184, June 2017, DOI: 10.1109/TPEL.2016.2598173.

[58] G. Liu, D. Li, Y. Jang and J. Zhang, "Over 300kHz GaN device based resonant bidirectional DCDC converter with integrated magnetics," *2016 IEEE Applied Power Electronics Conference and Exposition (APEC)*, 2016, pp. 595-600, DOI: 10.1109/APEC.2016.7467932.

[59] Y. Jang, M. M. Jovanović, J. M. Ruiz, M. Kumar and G. Liu, "Implementation of 3.3-kW GaN-based DC-DC converter for EV on-board charger with series-resonant converter that employs combination of variable-frequency and delay-time control," *2016 IEEE Applied Power Electronics Conference and Exposition (APEC)*, 2016, pp. 1292-1299, DOI: 10.1109/APEC.2016.7468035.

[60] S. Ryu, D. Kim, M. Kim, J. Kim and B. Lee, "Adjustable Frequency–Duty-Cycle Hybrid Control Strategy for Full-Bridge Series Resonant Converters in Electric Vehicle Chargers," in *IEEE Transactions on Industrial Electronics*, vol. 61, no. 10, pp. 5354-5362, Oct. 2014, DOI: 10.1109/TIE.2014.2300036.

[61] W. -Y. Choi, M. -K. Yang and H. -S. Cho, "High-Frequency-Link Soft-Switching PWM DC–DC Converter for EV On-Board Battery Chargers," in *IEEE Transactions on Power Electronics*, vol. 29, no. 8, pp. 4136-4145, Aug. 2014, DOI: 10.1109/TPEL.2013.2288364.

[62] J. Min and M. Ordonez, "Bidirectional Resonant CLLC Charger for Wide Battery Voltage Range: Asymmetric Parameters Methodology," in *IEEE Transactions on Power Electronics*, vol. 36, no. 6, pp. 6662-6673, June 2021, DOI: 10.1109/TPEL.2020.3033982.

[63] H. Li, S. Wang, Z. Zhang, J. Tang, X. Ren and Q. Chen, "A SiC Bidirectional LLC On-Board Charger," *2019 IEEE Applied Power Electronics Conference and Exposition (APEC)*, 2019, pp. 3353-3360, DOI: 10.1109/APEC.2019.8722324.

[64] H. Wang and Z. Li, "A PWM LLC Type Resonant Converter Adapted to Wide Output Range in PEV Charging Applications," in *IEEE Transactions on Power Electronics*, vol. 33, no. 5, pp. 3791-3801, May 2018, DOI: 10.1109/TPEL.2017.2713815.

[65] IEC, "European standard iec 61851-23: 2014. electric vehicle conductive charging systemapart 23: Dc electric vehicle charging station," 2014.

[66] L. Costa, G. Buticchi and M. Liserre, "A Fault-Tolerant Series-Resonant DC–DC Converter," in *IEEE Transactions on Power Electronics*, vol. 32, no. 2, pp. 900-905, Feb. 2017, DOI: 10.1109/TPEL.2016.2585668.

[67] F. Grazian, T. B. Soeiro and P. Bauer, "Inductive Power Transfer based on Variable Compensation Capacitance to Achieve an EV Charging Profile with Constant Optimum Load," in *IEEE Journal of Emerging and Selected Topics in Power Electronics*, 2022, DOI: 10.1109/JESTPE.2022.3188060.

[68] K. Venkatachalam, C. R. Sullivan, T. Abdallah and H. Tacca, "Accurate prediction of ferrite core loss with nonsinusoidal waveforms using only Steinmetz parameters," *2002 IEEE Workshop on Computers in Power Electronics*, 2002. Proceedings., 2002, pp. 36-41, DOI: 10.1109/CIPE.2002.1196712.

[69] S. Rivera, S. Kouro, S. Vazquez, S. M. Goetz, R. Lizana and E. Romero-Cadaval, "Electric Vehicle Charging Infrastructure: From Grid to Battery," in *IEEE Industrial Electronics Magazine*, vol. 15, no. 2, pp. 37-51, June 2021, DOI: 10.1109/MIE.2020.3039039.

[70] S. Rivera et al., "Charging Infrastructure and Grid Integration for Electromobility," in *Proceedings of the IEEE*, vol. 111, no. 4, pp. 371-396, April 2023, DOI: 10.1109/JPROC.2022.3216362.